J Mater Sci: Mater Electron (2015) 26:1217–1224
DOI 10.1007/s10854-014-2528-4

Effect of nitrate concentration on the electrochemical growth and properties of ZnO nanostructures

L. Mentar · O. Baka · M. R. Khelladi · A. Azizi · S. Velumani · G. Schmerber · A. Dinia

Received: 17 September 2014 / Accepted: 17 November 2014 / Published online: 25 November 2014

Abstract Zinc oxide (ZnO) nanostructures were deposited under potentiostatic control on indium tin oxide coated glass substrate from an aqueous solution containing zinc nitrates. Voltammograms were recorded to determine the optimal potential region for the deposition of ZnO. The deposition was carried out at various concentrations of Zn^{+2} and constant bath temperature (65 °C). The nucleation and growth kinetics at the initial stages of ZnO studied by current transients indicated a 3D island growth (Volmer–Weber). It is characterized by an instantaneous nucleation mechanism followed by diffusion-limited growth. The Mott–Schottky measurements, the flat band potential and the donor density for the ZnO nanostructures were determined. The morphological, structural, and optical properties of the nanostructures have been investigated. Scanning electron microscopy images showed different sizes and morphologies of the nanostructures which depends on the concentrations of Zn^{+2}. X-ray diffraction study confirms the wurtzite phase of the ZnO nanostructures with high crystallinity. UV–visible spectra showed a significant optical transmission (up to 90 %), which decreased with Zn^{2+} concentrations. The energy band gap values have been estimated to be in the range 3.36–3.54 eV.

L. Mentar · O. Baka · M. R. Khelladi · A. Azizi (✉)
Faculté de Technologie, Laboratoire de Chimie, Ingénierie Moléculaire et Nanostructures, Université Sétif 1, 19000 Sétif, Algeria
e-mail: aziziamor@yahoo.fr

S. Velumani
Centro de Investigacion y de Estudios Avanzados del I.P.N (CINVESTAV), Instituto Politecnico Nacional, Av. # 2508, Col. San Pedro Zacatenco, 07360 Mexico, D.F, Mexico

G. Schmerber · A. Dinia
Institut de Physique et Chimie des Matériaux de Strasbourg (IPCMS), UMR 7504 CNRS-Université de Strasbourg, 23 rue du Loess, B.P. 43, 67034 Strasbourg Cedex 2, France

1 Introduction

The synthesis of semiconductor crystals with well-defined shapes, sizes, and structures has attracted extraordinary interest in order to realize their unique properties that not only depends on their chemical composition, but also on their shape, structure, phase, size, and size distribution [1, 2]. Among various synthesis methods, electrochemical deposition represents a simple and inexpensive solution-based method for synthesis of semiconductor nanostructures. Zinc oxide (ZnO)-based semiconductors have been investigated as promising materials for advanced electronic and optoelectronic devices due to their interesting physical and chemical properties [3, 4]. It is an established fact that the electrodeposition of ZnO is a versatile growth method and various nanostructures can be easily designed by this technique. Due to its simplicity and low cost, there has been growing interest in ZnO nanostructures fabricated by electrodeposition methods, and a range of morphologies and growth conditions have been reported [5–10]. These nanostructures have attracted considerable interest owing to their excellent electronic and optical properties [11–13]. In effect, ZnO has a band gap of 3.37 eV at room temperature with a high exciton binding energy of 60 meV. Hence, ZnO has been considered as a material of choice for use in short-wavelength light-emitting diodes (LEDs), laser diodes, organic LEDs [14], as sensors [15], photovoltaic cells [16], LEDs [17] and nanogenerators [18].

Consequently, in recent years, there has been extensive interest in synthesizing various ZnO nanostructures, including nanorods [18, 19], nanowires [20], nanoneedles [21], nanocombs [22], nanoplates [23] and nanobelts [24]. The properties and applications of ZnO-derived devices are strongly dependent on the size, shape and orientation. Therefore, the precision control of the morphology of ZnO crystals is a matter of considerable importance for tailoring their physical properties and improves device performance exploring the potential oxide material [25–28].

The growth of nanostructures was controlled by the deposition parameters such as electrolyte bath composition, bath temperature, pH, deposition potential or deposition current density, agitation or electrodeposition dynamics [29]. A small variation in the electrodeposition parameters conducts remarkable changes in the morphology and crystallography of the ZnO thin films [29, 30]. Consequently, in this work we studied the effect of concentrations of Zn^{+2} on the properties of ZnO nanostructures.

2 Experimental

ZnO nanostructures were prepared by electrodeposition onto polycrystalline indium tin oxide (ITO)-coated conducting glass substrate with an exposed area of 1 × 1 cm^2 (10–20 Ω/cm^2 sheet resistance). The substrates were sonicated in acetone, and rinsed in isopropanol and deionized water to remove any organic contaminations. All the depositions were made in a three-electrodes cell containing Pt as a counter electrode, saturated calomel electrode (SCE) as reference, and ITO-coated glass as a working electrode. The nanostructures were deposited in a potentiostatic mode, using a computer-controlled potentiostat/galvanostat (Voltalab 40) as a potential source. All ZnO nanostructures were deposited from aqueous solutions of zinc nitrate aqueous solution with 1 M KNO_3. The pH was fixed at 6.5. All the solutions were prepared using type I water (Milli-Q). In this work, the bath temperature was fixed at 65 °C, and the concentrations of $Zn(NO_3)_2$ were varied from 60 to 120 mM. Cyclic voltammetry (CV) measurements were conducted to determine the deposition potentials of the thin films.

Morphological characterization was performed by field emission scanning electron microscopy (FESEM, JEOL JSM-6700F). Phase identification and crystallographic structure determination were carried out using X-ray diffraction (XRD) on a Philips X-Pert Pro diffractometer with $CuK\alpha_1$ incident radiation source (λ = 1.54056 Å) in a θ–2θ geometry. The optical properties of the ZnO nanostructures were measured with an UV–Vis-NIR spectrophotometer (Shimadzu UV-3150).

3 Results and discussion

3.1 Synthesis of ZnO nanostructures

During the electrodeposition process of ZnO, nitrates ions are reduced to nitrite ions in the presence of Zn^{2+} adsorbed on the surface of the substrate. Consequently, excess hydroxide ions are produced, increasing the local pH. This pH increase facilitates the formation of $Zn(OH)_2$ on the working electrode, which spontaneously decomposes to ZnO at temperatures above 50 °C [31, 32]:

$$NO_3^- + H_2O + 2e^- \rightarrow NO_2^- + 2OH^- \quad (1a)$$

$$Zn^{2+} + 2OH^- \rightarrow Zn(OH)_2 \quad (1b)$$

$$Zn(OH)_2 \rightarrow ZnO_{\downarrow} + H_2O \quad (1c)$$

The complete balanced reaction is as follow:

$$Zn^{2+} + NO_3^- + 2e^- \rightarrow ZnO + NO_2^- \quad (2)$$

According to this mechanism, the formation rate of $Zn(OH)_2$ is affected by applied current density, Zn^{2+} concentration [Zn^{2+}]. The crystallization is accompanied by dehydration which depends on the deposition temperature (bath temperature). In our case, the applied potential was fixed at −1.3 V versus SCE, and deposition temperature at 65 °C and [Zn^{2+}] were changed to systematically examine the electrochemical, morphological and structural properties of electrodeposited ZnO.

In order to study the effect of Zn^{2+} concentration in the electrochemical behavior of ZnO electrodeposition, the CV was investigated from solution at different concentrations of Zn^{2+}. Figure 1a shows the CV performed in the potential range 0 to −1.2 V versus SCE onto ITO-covered glass substrate from (60 to 120 mM) zinc nitrate aqueous solution with 1 M KNO_3 at 70 °C and pH 6.5. The potential scan was initiated in the negative direction from the open circuit potential at scan rate of 20 mV s^{-1}. Cathodic current due to reduction of NO_3^- emerged at a potential of −0.68 V versus SCE and rapidly increased at around −0.87 V (Fig. 1a).

From the CV scans, the variation of Zn^{2+} concentration influences the reaction, thus leading to an increase in ZnO nanostructure growth rate. The effects of Zn^{2+} concentration on the growth rate of ZnO deposition can be seen in Fig. 1b. As Zn^{2+} concentration increases in the electrolyte, the deposition rate increases and there is an equivalent rise in the growth rate. The deposition rates ranging from 6.27 to 9.25 nm/s are obtained depending on the Zn^{2+} concentration from 60 to 120 mM. From this Fig. 1b, it is well-known that the deposition rate of ZnO nanostructures could be controlled by adjusting the Zn^{2+} concentration. The changes in the ZnO growth rate related to Zn^{2+} concentration in the electrolyte correlate well with the CV curve.

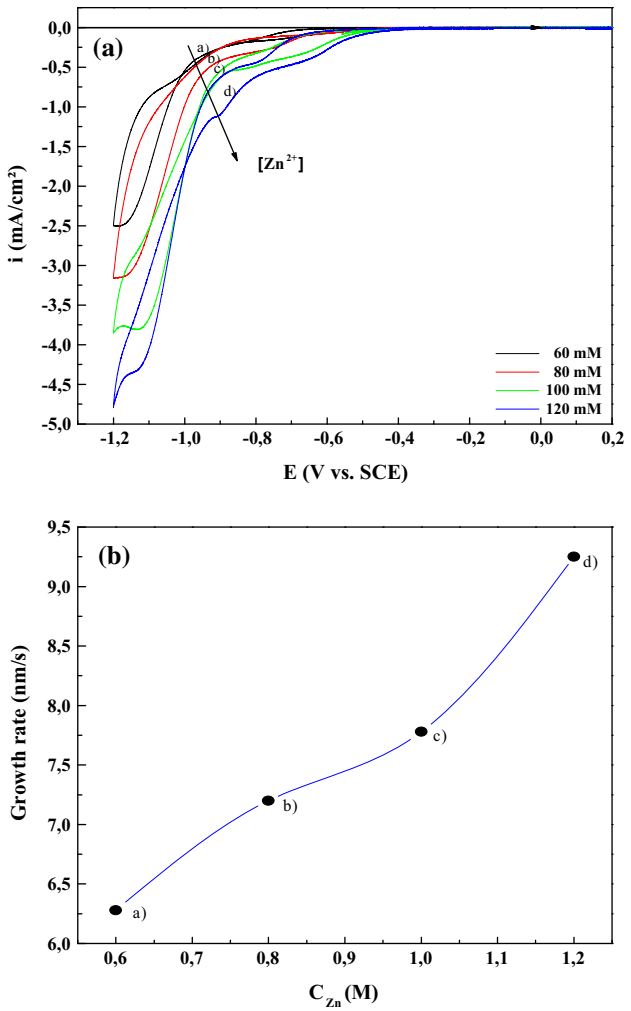

Fig. 1 **a** Cathodic scan of (60–120 mM) $Zn(NO_3)_2$ with 1 M KNO_3 aqueous solution at 65 °C on ITO electrode, the scan rate was 20 mV s^{-1}. **b** Growth rate of ZnO nanostructures as a function of Zn^{2+} concentration in the growth solution

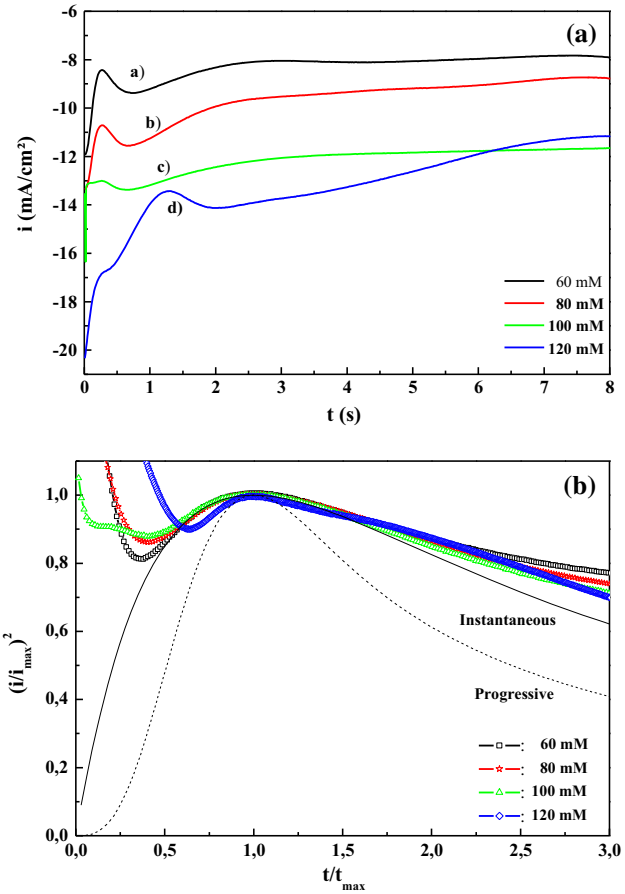

Fig. 2 **a** Current transients for ZnO deposition on ITO substrates with the concentration of Zn^{2+} ions ranging from 60 to 120 mM. **b** Normalized transients $(i/i_{max})^2$ versus t/t_{max} from Fig. 2a. In each plot, the *full line* corresponds to the calculated curve for instantaneous nucleation and diffusion-limited growth, and the *dotted line* represents the calculated curve for progressive nucleation and diffusion-limited growth

The growth rate curve indicates that the deposition process becomes too fast resulting in an uniform nanostructures growth at very large current densities due to high Zn^{2+} concentrations (120 mM). Similar reports of increased current density observed in the electrochemical growth of doped ZnO elsewhere [33, 34].

Chronoamperometric measurements were made at various bath compositions to explore the nucleation and growth process associated with electrochemical deposition of ZnO. Figure 2a represents a series of current–time transients for the deposition of ZnO in zinc nitrate bath at different concentrations. The shape is typical of a 3D electrocrystallization growth process; the current density decreases with increasing Zn concentration. This result can be explained at least in part by the well-known suppression effect of nitrate concentration on the ZnO growth rates. The three-dimensional island growth of each crystal rapidly increases the active surface area. The current passes through a maximum during the coalescence process. In order to determine whether the nucleation is progressive or instantaneous at each Zn concentration, $(i/i_{max})^2$ versus t/t_{max} were compared to the Sharifker–Hills model, the instantaneous nucleation models agreed with the experiment (Fig. 2b).

The conduction type, the flat band (E_{fb}), and the estimated donor densities of ZnO were determined using Mott–Schottky (M–S) measurements with $1/C^2$ versus E at a fixed frequency of 20 kHz. The capacitance-potential measurements are presented as a M–S plot following the equation below [35]:

$$\frac{1}{C^2} = \frac{2}{N_D e \varepsilon_0 \varepsilon}\left[(E - E_{fb}) - \frac{kT}{e}\right] \quad (3)$$

where C is the space charge capacitance in the semiconductor, N_D is the hole carrier density, e is the elemental

charge value, ε_0 is the permittivity of the vacuum of free space (8.859×10^{-14} F cm^{-1}), ε is the relative permittivity of the semiconductor (ε of ZnO is 8.5), E is the applied potential, E_{fb} is the flat band potential, T is the temperature, and k is the Boltzmann constant.

The M–S plot (Fig. 3) of the samples deposited in the electrolyte containing different Zn^{2+} concentrations, shows a positive slope, which confirms the n-type semiconducting behavior of ZnO [36]. Thus from Fig. 3, the flat band potential for all the samples and the donor densities calculated from the slope $\left(=\frac{2}{\varepsilon\varepsilon_0 eN_D}\right)$ and intercept at $C = 0$, are estimated. Table 1 listed the carrier concentration obtained from the linear fitting of the curves. The carrier density fluctuates from 4.05 to 1.73×10^{20} cm^{-3}. It is shown that carrier concentration decreases with the increase in Zn^{2+} concentration in ZnO nanostructures. The higher donor densities of the samples clearly indicate that there is n-doping for the ZnO nanostructure which is in good agreement with reported carrier concentrations for ZnO [37]. The resources of carrier are due to the oxygen vacancies via nitrate solutions, and the mobility was influenced by a few scattering mechanisms. In addition, the extrapolation of the linear regions in these plots permits to estimate the flat band potential (E_{fb}). Table 1 also summarizes the E_{fb} values for different Zn^{2+} concentrations of zinc nitrate aqueous solution.

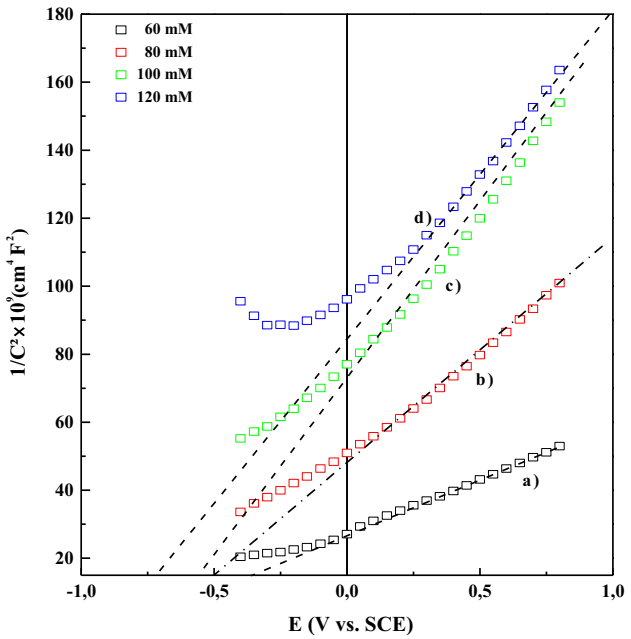

Fig. 3 Mott–Schottky plot for electrodeposited ZnO nanostructures in different concentrations of $Zn(NO_3)_2$ (60–120 mM) + 1 M KNO_3 solution obtained at 20 kHz. The corresponding flat band potential values are indicated. The *lines* were simply drawn through the data points

Table 1 Data of the ZnO nanostructures: bath composition, conditions for electrodeposition, flat band potential and carrier density

Concentration (mM)	E_{fb} (V vs. SCE)	$N_D \times (10^{20}$ cm$^{-3})$
60	−0.843	4.05
80	−0.730	2.50
100	−0.691	1.60
120	−0.901	1.73

3.2 Morphological and structural properties

It is well established that the electrodeposition of nanostructures is a versatile growth method and many various nanostructures can be easily designed by the technique. We obtained different morphologies of ZnO nanostructures using different $Zn(NO_3)_2$ concentrations. Figure 4 displays FESEM images of ZnO nanostructures obtained from four different concentrations of Zn^{2+} for a constant deposition time (15 min). At 60 mM concentration of Zn^{2+}, the substrate is not totally covered and the morphology is not homogeneous with few hexagonal structures having random orientations (inset Fig. 4a). All grains deposited at 80 mM have hexagonal structure oriented perpendicularly to the substrate; along the (001) orientations, which is in agreement with the XRD analysis. At 100 mM (Fig. 4c), a net rod morphology with random orientations are observed. After the increase of Zn^{2+} concentration in the electrolytic to 120 mM, the film morphologies change substantially and a cluster-like surface is formed as shown in Fig. 4d. In order to correlate the microstructure and the distribution of O and Zn, elemental map and spectrum of the same region were recorded. Elemental mapping of the ZnO sample deposited at 80 mM concentrations of Zn^{2+} (Fig. 4b), revealed an uniform distribution of various ions in the sample (Fig. 4e, f).

The phase purity and crystalline structure of ZnO samples were also characterized using XRD. Figure 5 shows the XRD patterns of ZnO samples deposited at different bath $Zn(NO_3)_2$ concentrations. The sharp and intense diffraction peaks indicate that the film is highly crystalline. All the diffraction peaks in Fig. 5 can be indexed as the wurtzite-type ZnO (JCPDS no. 00-036-1451, space group $P6_3mc$, a = 3.250 Å, c = 5.207 Å). No peak of impurities was observed, indicating that the final product is a pure compound. There is only a strong (002) peak from the film prepared using the solution with a zinc concentration of 80 mM, which has already been confirmed by FESEM image in Fig. 4. In contrast, the film deposited with a high zinc concentration had significantly lower (002) peak. These results indicate that the changes in grain orientation and microstructure were attributable to changes in the growth mechanism induced by the variation of zinc concentrations.

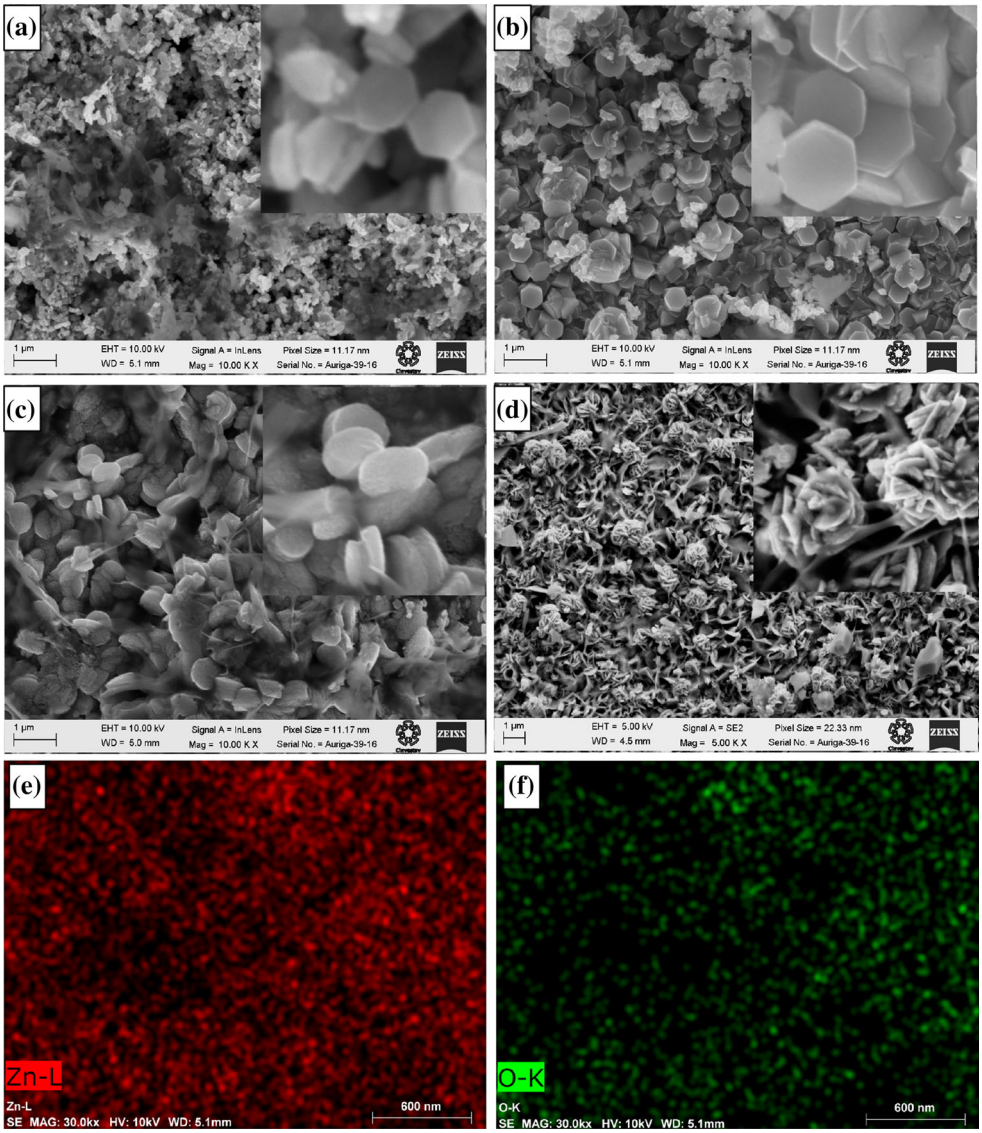

Fig. 4 FESEM images of ZnO nanostructures deposited at different concentrations of Zn^{2+}: **a** 60 mM, **b** 80 mM, **c** 100 mM and **d** 120 mM. The *inset* shows the corresponding high magnification FESEM images. **e**, **f** Elemental mapping of sample (**b**) showing the presence of (**e**) Zn and (**f**) O ions, respectively

Furthermore, the sharp peaks indicate that the samples are well crystallized. This indicates that the electrodeposition method could also be useful for the preparation of crystalline ZnO nanostructures. The crystallites size and microstrain for the electrodeposited ZnO nanostructures were obtained from the XRD diffraction peaks, which can be expressed as a linear combination of the particles size, D and microstrain ε as given below. The average crystallites size can be calculated with the Scherrer equation using the (002) peak line [38]:

$$D = \frac{0.9\,\lambda}{\beta\,\cos\,\theta} \tag{4}$$

where D is the crystallites size, λ is the incident X-ray wavelength, θ the Bragg angle and β is the full-width at half-maximum (FWHM) of the diffraction peak. Table 2 shows the values of crystallites size and other microstructural parameters. In this table, the crystallites size is increased gradually with increase in concentration of nitrate bath from 60 to 120 mM. We attribute that crystallites size increases with increase in deposition rate. The crystallites size can be controlled simply by varying the concentration of nitrate bath.

The origin of the microstrain is related to the lattice misfit, which in turn depends upon the deposition conditions. The microstrain ε is calculated using the relation [39],

$$\varepsilon = \frac{\beta\,\cos\,\theta}{4} \tag{5}$$

Table 2 shows microstrain with various concentrations of nitrate bath. Initially, the microstrain decreases slowly with increasing concentration of nitrates and a minimum value of 0.001 is obtained at 120 mM.

The dislocation density (δ) was defined as the length of dislocation lines per unit volume (lines/m^2). The

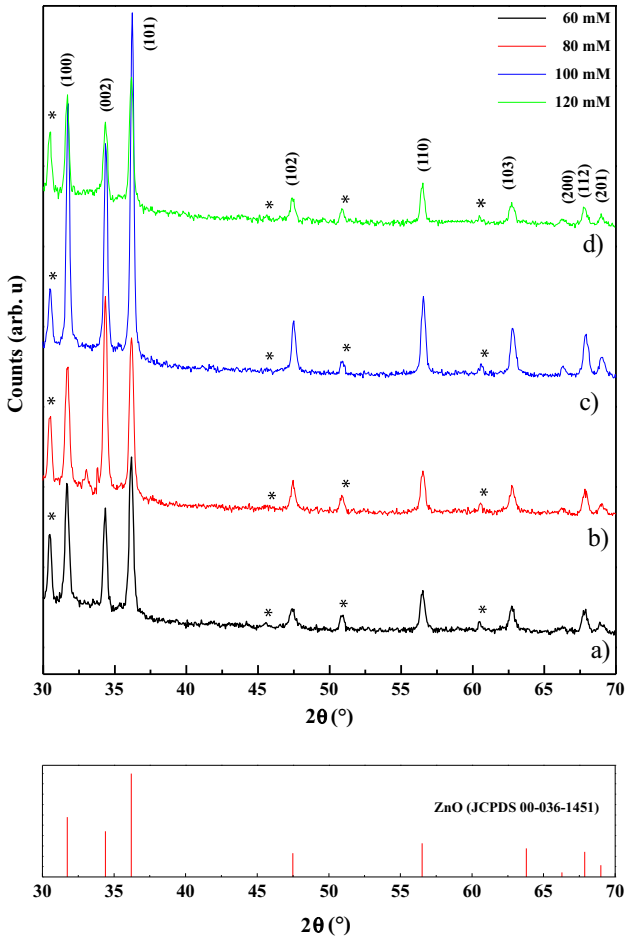

Fig. 5 XRD patterns of ZnO nanostructures at various concentrations of $Zn(NO_3)_2$: **a** 60 mM, **b** 80 mM, **c** 100 mM and **d** 120 mM with 1 M KNO_3 at pH 6.5. The *asterisk* assigned the ITO substrates diffraction peaks

Table 2 Effects of concentrations of Zn^{2+} ions on the microstructural properties of ZnO nanostructures

C (mM)	2θ (°)	Lattice constant (Å)		D (nm)	ε ($\times 10^{-3}$)	δ ($\times 10^{14}$ lines/m^2)
		a	c			
60	34.33	3.196	5.221	56.97	2.3	3.081
80	34.34	3.195	5.218	57.56	1.9	3.018
100	34.37	3.193	5.214	68.52	1.2	2.129
120	34.39	3.195	5.218	70.46	1.0	2.014

dislocation density (δ) of the films was estimated using the equation [40],

$$\delta = \frac{1}{D^2} \tag{6}$$

Since δ is a measure of the amount of defects in a crystal, these values of δ are summarized in Table 2. From this table, these structural parameters are crucially dependent on the concentration of nitrates in the electrolyte solution. An increase in nitrate concentration results in an increase in crystallites size. Increasing the nitrate concentration from 60 to 120 mM significantly decreases the microstrain of the film. Microstrain increase is caused by increase in nitrate concentration. In addition, the small value of δ obtained for 80 and 100 mM concentrations of Zn^{2+} confirmed that there is an improvement in the crystallinity of ZnO nanostructures.

From FESEM and XRD observations, it appears that the shape, size, crystallinity and preferential orientation of ZnO nanostructures depend on the bath concentration.

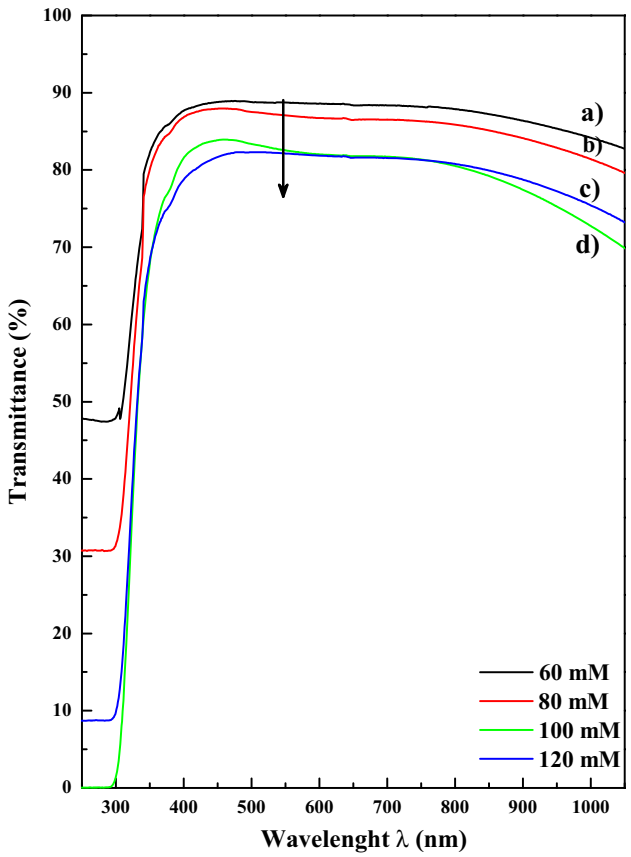

Fig. 6 UV–Vis transmittance spectra of ZnO nanostructures deposited at different concentrations of $Zn(NO_3)_2$: **a** 60 mM, **b** 80 mM, **c** 100 mM and **d** 120 mM

3.3 Optical properties of ZnO nanostructures

To study the influence of the different concentrations of Zn^{2+} ions on the optical properties of the grown ZnO nanostructures, transmittance measurements were conducted and the results are presented in Fig. 6.

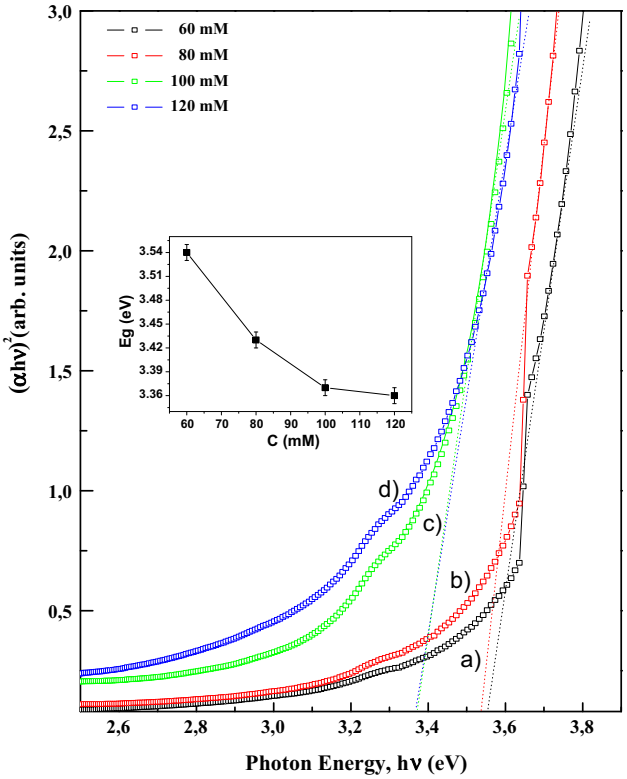

Fig. 7 Plot $(\alpha h\nu)^2$ versus hν for ZnO nanostructures deposited on conductive ITO electrode at different concentrations of Zn^{2+} ions. The band gap values obtained by extrapolating the linear part of the curves are also shown. The *inset* shows the variation of the optical band gap as a function of concentration of $Zn(NO_3)_2$

Transmittance in the visible range (400–800 nm) for the electrodeposited nanostructures is 80–90 % for all concentrations of $Zn(NO_3)_2$; and a sharp absorption edge was observed at around 380 nm. The drop in transparency in the infrared region shown by all films is due to their high charge carrier concentration [41]. It is well-established fact that the optical transmission in the visible range is important for transparent conductive oxide applications such as solar cell windows.

The energy band gap (E_g) for ZnO nanostructures was evaluated by using the Tauc plot [42]. A linear relationship between $(\alpha h\nu)^2$ and hν ensures the direct allowed transition in ZnO. The value of E_g is determined from the intercept of the straight-line portion at the horizontal axis when $\alpha = 0$. This method is known to be accurate for the estimation of the Eg of ZnO nanostructures [43–45]. The relationship of $(\alpha h\nu)^2$ and photon energy $h\nu$ for ZnO nanostructures deposited at different concentrations of Zn^{2+} is shown in Fig. 7. The values of E_g for ZnO nanostructures are estimated to be between 3.36 and 3.54 eV (inset Fig. 7). These E_g values of ZnO nanostructures obtained by electrodeposition are similar to other reports [46].

4 Conclusion

In this study we have presented an electrochemical deposition method and studied the properties of ZnO nanostructures on ITO surfaces from aqueous zinc nitrate aqueous solution. The effects of Zn^{2+} concentrations on electrodeposition process, nucleation-growth, morphology of microstructures and optical properties were investigated by means of CV, Mott–Schottky, FESEM, XRD and UV–Vis spectroscopy techniques. The experimental results show that the electrochemical behavior of ZnO electrodeposits varied with the concentrations of Zn^{2+} and the mechanism for formation of the film in the early deposition stages was proceeded according to the three dimensional (3D) instantaneous nucleation followed by diffusion-limited growth rather than an instantaneous one. The Mott–Schottky plot shows that all the nanostructures are n-type semiconductors, and presented the electron carrier density between 1.60 and 4.05 × 10^{20} cm^{-3} when the Zn^{2+} concentration was varied between 60 and 120 mM. FESEM images reveal that the Zn^{2+} concentrations have a very significant influence on the surface morphology, shape and size of the crystallites of ZnO. XRD measurements reveal a wurtzite structure with improved crystallization state. It was established that the crystallites size varies with the Zn^{2+} concentrations from 57 to 70 nm. The optical band gap obtained through transmittance measurements is in the range of 3.36–3.54 eV. It is quite reasonable that the films synthesized by electrochemical method at various Zn^{2+} concentrations in nitrates aqueous solution can generate a high potential for photovoltaic applications in the near future for ZnO nanostructures.

Acknowledgments The authors are grateful to the DGRSDT-MESRS of Algeria for the financial support through the PNR program (2011–2013).

References

1. H.T. Shi, L.M. Qi, J.M. Ma, H.M. Cheng, J. Am. Chem. Soc. **125**, 3450–3451 (2003)
2. X. Lan, J.Y. Zhang, H. Gao, T.M. Wang, Cryst. Eng. Comm. **13**, 633–636 (2011)
3. S. Tuzemen, E. Gur, T. Yildirım, G. Xiong, R.T. Williams, J. Appl. Phys. **100**, 103513 (2006)
4. L.J. Mandalapu, F.X. Xiu, Z. Yang, D.T. Zhao, J.L. Liu, Appl. Phys. Lett. **88**, 112108 (2006)
5. M.R. Khelladi, L. Mentar, A. Beniaiche, L. Makhloufi, A. Azizi, J. Mat. Sci. Mater. Electron. **24**, 153–159 (2013)
6. M.R. Khelladi, L. Mentar, M. Boubatra, A. Azizi, Mater. Lett. **67**, 331–333 (2012)
7. S. Chatterjee, S. Gohil, B. Chalke, P. Ayyub, J. Nanosci. Nanotechnol. **9**, 4792–4796 (2009)
8. F. Xu, Y.N. Lu, Y. Xie, Y.F. Liu, Mater. Des. **30**, 1704–1711 (2009)
9. A.I. Inamdar, S.H. Mujawar, V. Ganesan, P.S. Patil, Nanotechnology **19**, 325706 (2008)

10. T. Pauporte, E. Jouanno, F. Pelle, B. Viana, P. Aschehoug, J. Phys. Chem. C **113**, 10422–10431 (2009)
11. C.J. Lee, T.J. Lee, S.C. Lyu, Y. Zhang, H. Ruh, H. Lee, J. Appl. Phys. Lett. **81**, 3648–3650 (2002)
12. M.H. Huang, Y. Wu, H. Feick, N. Tran, E. Weber, P. Yang, Adv. Mater. **13**, 113–116 (2001)
13. Z.W. Pan, Z.R. Dai, Z.L. Wang, Science **291**, 1947–1949 (2001)
14. X. Fang, L. Zhang, J. Mater. Sci. Technol. **22**, 1–18 (2006)
15. Q. Wan, Q.H. Li, Y.J. Chen, T.H. Wang, X.L. He, J.P. Li, L. Lin, Appl. Phys. Lett. **84**, 3654–3656 (2004)
16. Y. Jouane, P. Lévêque, T. Heiser, S. Colis, G. Schmerber, C. Leuvrey, A. Dinia, Y.A. Chapuis, J. Mat. Chem. **22**, 1606–1612 (2012)
17. Y.R. Ryu, W.J. Kim, H.W. White, J. Cryst. Growth **219**, 419–422 (2000)
18. X. Wang, J. Song, Z.L. Wang, J. Mater. Chem. **17**, 711 (2007)
19. H. Yu, Z. Zhang, M. Han, X. Hao, F. Zhu, J. Am. Chem. Soc. **127**, 2378–2379 (2005)
20. L. Vayssieres, Adv. Mater. **15**, 464–466 (2003)
21. B. Cao, Y. Li, G. Duan, W. Cai, Cryst. Growth Des. **6**, 1091 (2006)
22. P. Yang, H. Yan, S. Mao, R. Russo, J. Johnson, R. Saykally, N. Morris, J. Pham, R. He, H. Choi, J. Adv. Funct. Mater. **12**, 323–331 (2002)
23. B. Illy, B.A. Shollock, J.L. MacManus-Driscoll, M.P. Ryan, Nanotechnology **16**, 320–324 (2005)
24. L.F. Xu, Q. Liao, J. Zhang, X. Ai, D. Xu, J. Phys. Chem. C **111**, 4549–4552 (2007)
25. Z.R. Tian, J.A. Voigt, J. Liu, M.A. Rodriguez, H. Konishi, H. Xu, Nat. Mater. **2**, 821–826 (2003)
26. Q. Li, K. Cheng, W.J. Weng, C.L. Song, P.Y. Du, G. Shen, G.R. Han, Nanoscale Res. Lett. **6**, 477–487 (2011)
27. K.S. Kim, H. Jeong, M.S. Jeong, G.Y. Jung, Adv. Funct. Mater. **20**, 3055–3063 (2010)
28. J.J. Dong, C.Y. Zhen, H.Y. Hao, J. Xing, Z.L. Zhang, Z.Y. Zheng, X.W. Zhang, Nanoscale Res. Lett. **8**, 378 (2013)
29. B.N. Illy, A.C. Cruickshank, S. Schumann, R. Da Campo, T.S. Jones, S. Heutz, M.A. McLachlan, D.W. McComb, D.J. Rileya, M.P. Ryan, J. Mater. Chem. **21**, 12949–12957 (2011)
30. J.D. Saunderson, R. Swanepoel, M.J. van Staden, Sol. Energy Mater. Sol. Cells **51**, 425–432 (1998)
31. T. Yoshida, D. Komatsu, N. Shimokawa, H. Minoura, Thin Solid Films **451**, 166–169 (2004)
32. S.J. Limmer, E.A. Kulp, J.A. Switzer, Langmuir **22**, 10535–10539 (2006)
33. O. Lupan, T. Pauporte, T.L. Bahers, I. Ciofini, B. Viana, J. Phys. Chem. C **115**, 1454–14558 (2011)
34. M. Kemell, F. Dartigues, Ritala M and Leskela. Thin Solid Films **434**, 20–23 (2003)
35. D.F. Watson, A. Marton, A.M. Stux, G.J. Meyer, J. Phys. Chem. B **107**, 10971–10973 (2003)
36. C.X. Xu, X.W. Sun, X.H. Zhang, L. Ke, S.J. Chua, Nanotechnology **15**, 856–861 (2004)
37. D. Pradhan, K. Susanta, S. Mohapatra, M. Tymen, K. Misra, T. Leung, Mater. Express **1**, 59–67 (2011)
38. B.D. Cullity, S.R. Stock, *Elements of X-Ray Diffraction*, 3rd edn. (Prentice Hall, Upper Saddle River, 2001)
39. K.L. Chopra, *Thin film phenomena* (McGraw-Hill, New York, 1969)
40. K. Ravichandran, G. Muruganantham, B. Sakthivel, Physica B **404**, 4299–4302 (2009)
41. D.S. Ginley, H. Hosono, D.C. Paine, *Handbook of Transparent Conductors* (Springer, London, 2010)
42. J. Tauc, in *Optical Properties of Solids* 22, ed. by F. Abeles (North Holland Pub, Amsterdam, 1970)
43. J. Xue, Q. Shen, W. Liang, X. Liu, L. Bian, B. Xu, Surf. Coat. Technol. **216**, 166–171 (2013)
44. S. Laidoudi, A.Y. Bioud, A. Azizi, G. Schmerber, J. Bartringer, S. Barre, A. Dinia, Semicond. Sci. Technol. **28**, 115005 (2013)
45. I. Soumahoro, R. Moubah, G. Schmerber, S. Colis, M. Ait Aouaj, M. Abd-lefdil, N. Hassanein, A. Berrada, A. Dinia, Thin Solid Films **518**, 4593–4596 (2010)
46. O. Baka, A. Azizi, S. Velumani, G. Schmerber, A. Dinia, J. Mat. Sci. Mater. Electron. **25**, 1761–1769 (2014)